NATURALLY LAYERED PEROVSKITE HETEROSTRUCTURES

Results and Report of the Ph.D. Activities - January 31st, 2022

Bruna Machado da Silva[1]

This work is being carried out under supervision of:
Bernardo Gonçalves Almeida[1]
and co-supervision of:
Armandina Maria Lima Lopes[2]
João Pedro Esteves de Araújo[2]

[1]*Departamento de Física da Universidade do Minho*
[2]*Instituto de Física de Materiais Avançados, Nanotecnologia e Fotónica*

brunasilva@fisica.uminho.pt

Abstract

Room temperature magnetoelectric (ME) compounds are rare and high-quality artificially multilayered ones are in general difficult and costly to produce. In this respect, Naturally Layered structures (NLP), such as the Ruddlesden-Popper phases or A/B-site ordered Double perovskites, where noncentrosymmetric arises from oxygen octahedra rotations and cation site order, offer an alternative route to achieve non-expensive and high-performance room temperature MEs. Moreover, due to their high sensitivity to lattice-distortions, their preparation in thin film form over crystalline substrates allows the manipulation of acentricity and adjusting of lattice, electric and magnetic interactions. As such, this work aims to produce novel NLP thin films on crystalline substrates, and they can also be guided by ab-initio calculations. Strain mediated control of their magnetic/electric response as well as its relevance for future energy-efficient electronic applications is the focus of this work. The planned study will lead to the development and exploration of new multiferroic magnetoelectric naturally layered perovskites with enhanced room temperature ME responses.

Contents

1. Research plan

The project aims to produce Naturally Layered Perovskite (NLP) nanostructured thin films, based on cation doped Ruddlesden-Popper $Ca_3Mn_{2-x}Ti_xO_7$ or double-perovskite $AA´NiMnO_6$, prepared over crystalline substrates. The main objective is to explore octahedral rotations and lattice distortions in these naturally layered oxides to obtain combined enhanced magnetization and polarization at room temperature. By using film-on-substrate geometries, the strain tuning and control of these distortions through interface engineering offers prospects for manipulation of acentricity and adjusting of lattice, electric and magnetic interactions. We thus aim to explore the role of strain as a parameter for tuning ferroelectricity and magnetization in NLP. Thin films will be prepared by Pulsed-Laser Deposition (PLD) in different substrates ($YAlO_3$, $SrTiO_3$, $LaAlO_3$) and substrate orientations to induce tensile/compressive strain. To further attain strain tuned control of the films magnetic and electric properties, piezoelectric crystalline (e.g., PMN-PT) substrates will be used. Specific objectives are:

- Synthesis of laser-ablated nanoscopic (10-200nm) thin films composed by Naturally Layered Perovskites over crystalline substrates. Systematic characterization of their structural, chemical and morphological properties towards building epitaxial films-on-substrate NLP nanostructures.
- Systematic characterization of the magnetic properties as a function of temperature and magnetic field. Study of the influence of strain on the magnetic ordering temperatures induced by varying the layer thicknesses and the substrates involved.
- Systematic characterization of the electric properties (impedance spectroscopy, P-E hysteresis cycles) of the films. Determination of the influence strain on NLP octahedral rotations and onset of polarization in these nanostructures.
- Studies of strain-induced/magnetic field-induced coupled multiferroic behavior. Develop new multiferroic magnetoelectric naturally layered perovskites nanostructures, towards enhanced room temperature ME responses.

The research timeline starts with the deposition and processing of the thin film nanostructures. They are followed by their structural, chemical and spectroscopic analysis to determine the optimal deposition conditions in light of their electric, magnetic and magnetoelectric characteristics.

At this moment, the proposed work was carried out, specifically the deposition by PLD and structural, electric and magnetic characterization of the $Ca_3Mn_2O_7$ thin films on crystalline substrates. Also, there are samples selected for the magnetoelectric measurements. Based on the knowledge obtained, deposition conditions of $Ca_3Ti_2O_7$ and $Ca_{2.9}Sr_{0.1}Ti_2O_7$ thin films are being studied.

The work developed in $Ca_3Mn_2O_7$ systems was orally presented at the following conferences:

- 22ª Conferência Nacional de Física (2020);
- JEMS 2020 - Joint European Magnetic Symposia (2020);
- 4th Doctoral Congress in Engineering (2021);
- INTERMAG 2021 Conference (2021);
- 2021 Joint ISAF-ISIF-PFM Virtual Conference (2021);
- Annual MAP-fis Conference (2021);
- Nanotech France 2021 International Conference and Exhibition (2021);
- Smart Materials and Surfaces - SMS 2021 Conference and Exhibition (2021).

Also, a poster was prepared for the Workshop of the Laboratory for Physics of Materials and Emerging Technologies (2021). Finally, a scientific paper with the most relevant results obtained so far is currently being finalized.

2. Activities developed and results

Initially, the system chosen to start the work was the Ruddlesden-Popper $Ca_3Mn_2O_7$ system over $SrTiO_3$ and $SrTiO_3$:Nb substrates. The PLD system was used to produce the thin films and deposition conditions were studied. The structural, dielectric and magnetic properties of the produced $Ca_3Mn_2O_7$ thin films were also studied. Based on the knowledge obtained previously, systems of $Ca_3Ti_2O_7$ and $Ca_{2.9}Sr_{0.1}Ti_2O_7$ are being studied to obtain the PLD conditions for thin films production. This section presents the results obtained so far for $Ca_3Mn_2O_7$ thin films.

2.1. Tricalcium dimanganese heptaoxide

The tricalcium dimanganese heptaoxide ($Ca_3Mn_2O_7$) hybrid improper ferroelectric compound has a crystal structure that presents layers of corner-sharing MnO_6 octahedra, with two layers of $CaMnO_3$ for every sheet of CaO. At high temperatures $Ca_3Mn_2O_7$ is paraelectric, presenting the centrosymmetric I4/mmm structure [1]. As the temperature decreases, the $Ca_3Mn_2O_7$ paraelectric state can change to a ferroelectric $A2_1am$ structure, due to the combination of the rotations and tilt distortions of the oxygen octahedra [2]. That same lattice tilt distortions can modify the magnetic structure and the same rotations can produce a linear magnetoelectric coupling [2,3]. Nevertheless, the magnetic order develops at low temperatures, $T_N \sim 115$ K [4], making it difficult to incorporate NLP in devices [3]. Therefore, for practical applications of these NLP, a set of pathways to raising the multiferroic properties towards room temperature is needed. In this respect, the high sensitivity of complex oxides to lattice-distortions [1,5] combined with interface and strain engineering [6–10] leads to new functionalities. For example, theoretical calculations predict that a strain-induced nonpolar-to-polar transition, with a critical tensile strain beyond which the polar nature suddenly emerges, might be observed in $Ca_3Mn_2O_7$ and $Sr_3Zr_2O_7$ thin films through epitaxial strain [9]. Then, the formation of film-on-substrate structures allows to control and enhance the films magnetization and polarization [9,10] and, due to its simple structural characteristics (well-defined strain

states and well-defined interfaces), this geometry is particularly suited for device implementation. Nevertheless, so far, the production of thin films of $Ca_3Mn_2O_7$ has not been properly explored. Thus, the preparation conditions to obtain the envisaged $Ca_3Mn_2O_7$ thin films need to be studied and optimized and their electrical properties need to be characterized.

Thin films of calcium manganese oxide have been prepared by laser ablation over $SrTiO_3$ substrates. The conditions for the stabilization of the $Ca_3Mn_2O_7$ n = 2 Ruddlesden-Popper phase, with improper ferroelectricity and magnetic order, were studied, specifically, the oxygen pressures (from 10^{-3} to 10^{-1} mbar), laser fluences (1.4 - 3.4 J/cm^2), substrate temperatures (from room temperature to 730 ºC), and influence of post-deposition annealing. The corresponding structural, morphological and spectroscopic properties were correlated with their stabilized phases and preparation conditions. To further understand cooperative polar behaviour, polar order/disorder and onset of multiferroic correlations in the $Ca_3Mn_2O_7$ films, their dielectric properties were measured through impedance spectroscopy.

2.1.1. Results and Discussion

To obtain high-quality $Ca_3Mn_2O_7$ thin films and study the influence of the deposition conditions on the structure, a set of thin films was deposited on strontium titanate substrates ($SrTiO_3$) by pulsed laser deposition changing the deposition parameters, such as deposition temperature, oxygen pressure, laser fluence, target-substrate distance and influence of post-annealing. Table 1 presents the deposition conditions used to produce the samples.

Table 1: Deposition conditions of the produced thin films and respective conditions of post-annealing treatments at atmospheric pressure.

	Pulsed lased deposition				Post-annealing	
Sample	**T (ºC)**	**O_2 Pressure (mbar)**	**Laser fluence (J/cm^2)**	**$d_{target-sub}$ (cm)**	**T (ºC)**	**t (h)**
CMO2	700	0.05	2.3	4.5	N/A	N/A
CMO4	700	0.1	1.1	4.5		
CMO5	725	0.1	1.1	4.5		
CMO6	700	0.05	2.3	4.5		
CMO7	732	0.01	2.3	4.5		
CMO8	731	0.01	2.3	6		
CMO9	728	0.01	3.4	6		
CMO10	RT	0.01	3.4	6	730	2
CMO11	RT	0.01	3.4	6	730	10
CMO12	RT	0.01	3.4	3	730	2
CMO14	700	0.01	3.4	6	900	2
CMO15	700	0.01	3.4	6	800	2

Figure 1a and 1b show SEM micrographs obtained on samples CMO10 and CMO14 respectively. Both samples were produced under the same conditions, except for the deposition and post-annealing temperatures. Whereas sample CMO10 (Figure 1a) was deposited with the substrate at room temperature and subsequently annealed at 730 ºC. The sample CMO14 (Figure 1b) was deposited with the substrate at 730 ºC and annealed at 900 ºC for 2 h. As depicted in figure 1a, the film deposited and annealed at lower temperatures present a granular surface with an average grain size of 81 nm, determined from the SEM micrographs. However, for higher deposition and annealing temperatures the surface becomes progressively smoother, as seen in Figure 1b. Figure 2c shows the SEM cross-section for the CMO14 sample prepared with 50 minutes deposition time (sample shown in Figure 1b)). The thickness of the film is uniform along the samples area, showing some slight local variation attributable to roughness, giving an average

thickness of approximately 305 nm. This gives ~6.1 nm/min deposition rate. The sample presents a columnar growth morphology with column widths between 65 and 120 nm as shown in Figure 1d.

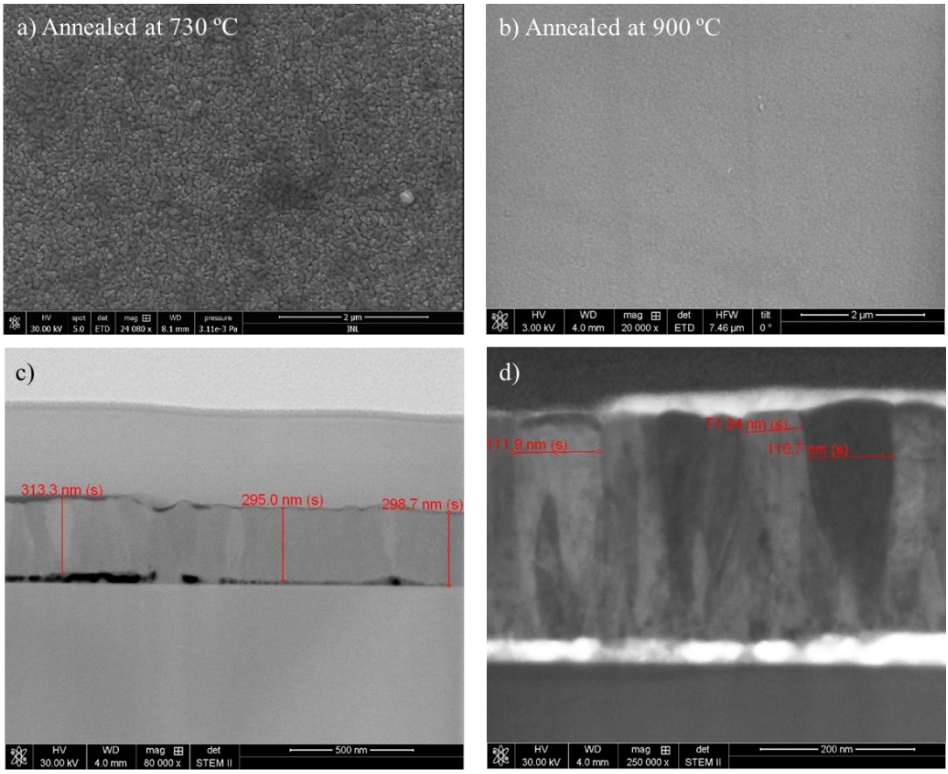

Figure 1: Scanning electron microscopy (SEM) micrographs of the surface of the samples: a) CMO10 deposited at room temperature and annealed at 730 ºC and b) CMO14 deposited at 700ºC and annealed at 900 ºC. c-d) Corresponding SEM cross-section micrograph of sample CMO14, presented in b) for a 50-minutes-deposition.

Figure 2 shows the X-ray diffraction measurements performed on the CMO films prepared with different deposition temperatures, laser fluences, oxygen pressures and target-substrate distances. No annealing was done in these samples. The vertical black and green lines indicate the peak positions of the $SrTiO_3$ substrate, with the cubic Pm3m structure (ICDD card number 35-734), and $CaMnO_3$ with the Pnma orthorhombic

structure [11]. Similarly, Figure 3 shows the X-ray diffraction measurements performed on the CMO films prepared with different deposition temperatures, oxygen pressures and target substrate distances, but with high pulse energies (high fluences) and with an annealing step after deposition. In Figure 2 and Figure 3, the vertical black lines indicate the peak positions of the $SrTiO_3$ substrate, with the cubic Pm3m structure and the vertical red and blue lines indicate the peak positions of $Ca_3Mn_2O_7$ with the Acaa orthorhombic structure [12] and of the ferroelectric $A2_1am$ orthorhombic structure [13], respectively.

Noticeably, in the parameter region that was used without annealing (Figure 2), namely, temperatures 700 – 730 ºC, oxygen pressures 0.01 – 0.1 mbar, laser fluences 1.4 – 2.3 J/cm^2 and target substrate distances 3 – 6 cm, the observed X-ray diffraction peaks are consistent with the stabilization of the $CaMnO_3$ orthorhombic Pnma phase in all the films. These films have also grown oriented, presenting the $CaMnO_3$ [001] direction perpendicular to the substrate plane.

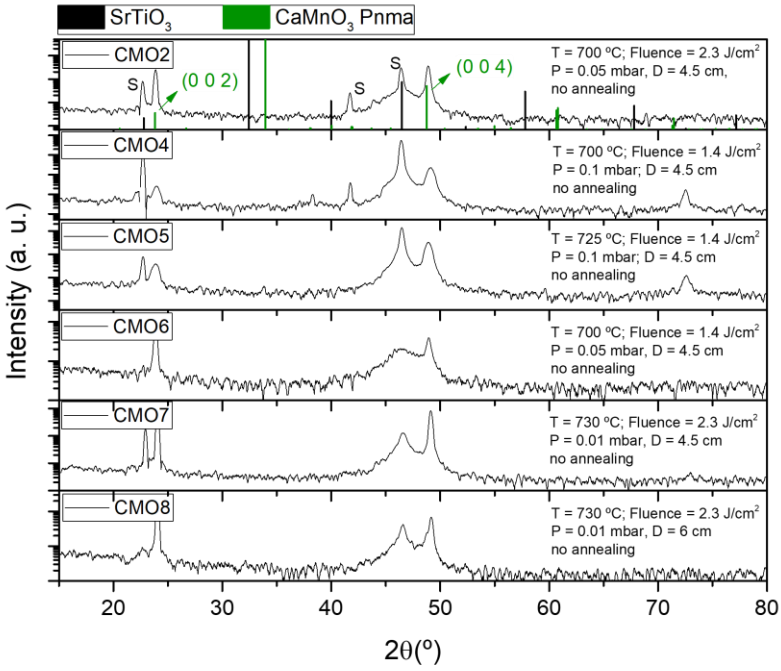

Figure 2: X-ray diffraction measured in the samples prepared with different oxygen pressures and deposition temperatures. The peaks marked with "S" are from the substrate. The green lines mark the reference diffraction peaks from the $CaMnO_3$ Pnma phase.

On the other hand, by decreasing the oxygen pressure, increasing the deposition temperature, increasing the laser fluence and increasing the post-deposition annealing temperature, the XRD indicates the stabilization of $Ca_3Mn_2O_7$ with the Acaa orthorhombic structure along with the ferroelectric $A2_1am$ phase of $Ca_3Mn_2O_7$ as shown in Figure 3. The decrease of the target-substrate distance was also observed to promote the formation of the $Ca_3Mn_2O_7$ phase, due to exposure of the film to more energetic species of the incident plume, for smaller distances.

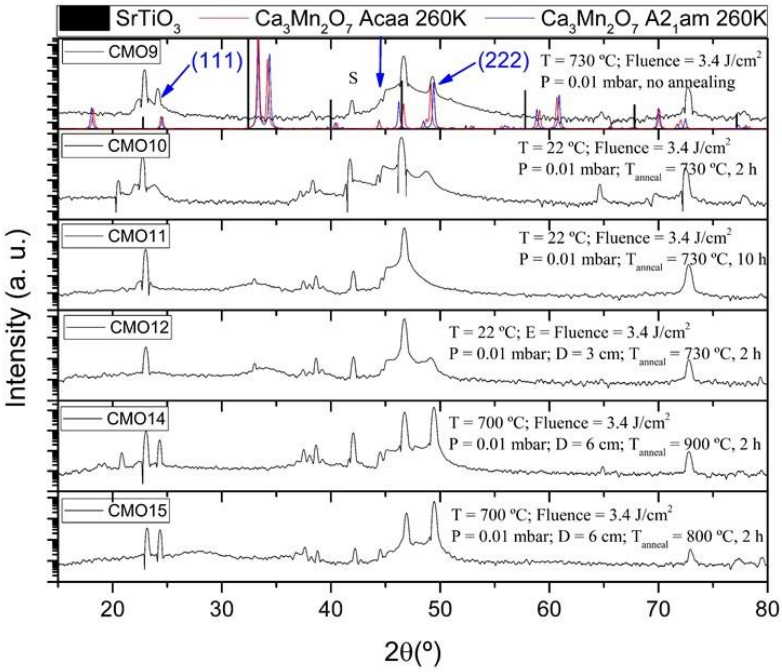

Figure 3: X-ray diffraction measured in the samples prepared with different oxygen pressures and deposition temperatures, but with higher laser pulse energies (high fluences) and with an annealing step after deposition. The peaks marked with "S" are from the substrate. The red and blue curves were obtained on bulk $Ca_3Mn_2O_7$ powder samples with Acaa or $A2_1am$ phases, respectively. The blue arrows mark the corresponding peaks observed in the films.

To further access the chemical and stoichiometric properties of the films and understand the conditions for the phases stabilization, energy dispersion X-ray spectroscopy measurements (EDX) were performed in the prepared films. The EDX spectra of the CMO10 and CMO14 samples are depicted in Figure 4. In the EDX of Figure 4, besides oxygen, the spectra present Sr and Ti due to the $SrTiO_3$ substrate, as expected. Additionally, peaks corresponding to Ca and Mn are also observed, due to the deposited thin films. No other elements were found indicating a high purity level of the samples.

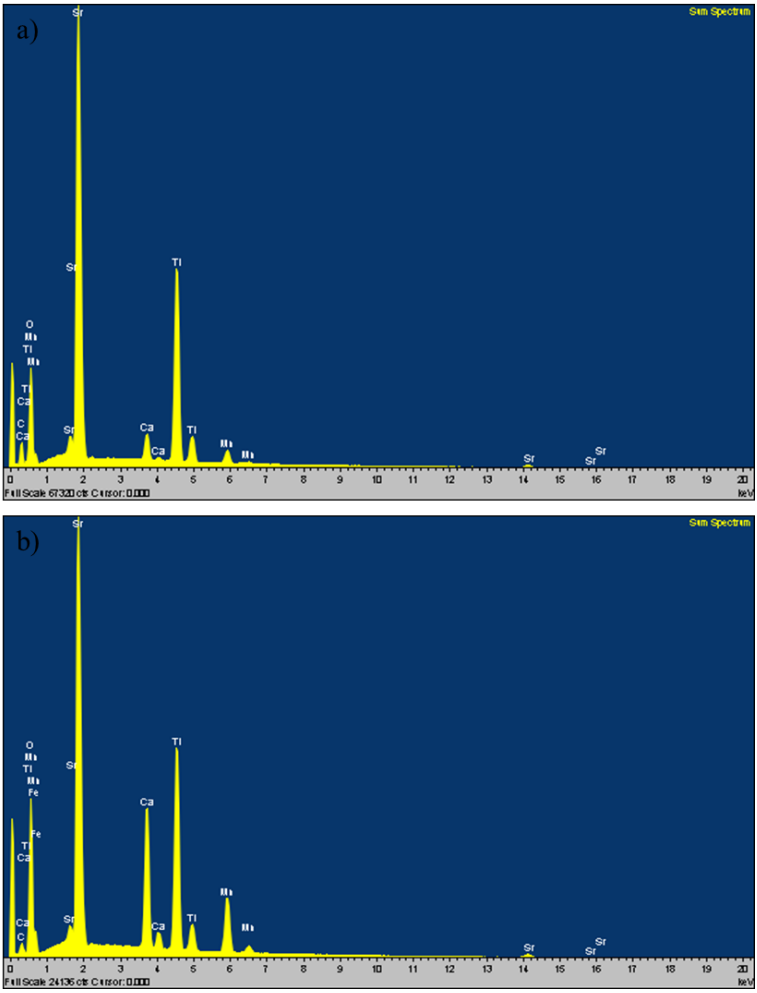

Figure 4: Energy-dispersive X-ray spectroscopy (EDS) spectrum measured in the samples a) CMO10 and b) CMO14.

Combining the XRD results obtained in the samples with different deposition conditions (Figures 2 and 3) and the chemical information obtained from the EDX characterization (Figure 4), the regions of values of the preparation parameters and the corresponding stabilized phases were determined. In this respect, the Ca/Mn atomic

percentages, determined from the EDX results for the samples with higher laser fluences (2.3 and 3.4 J/cm^2) are shown in Figure 5a. For $CaMnO_3$ the Ca/Mn ratio is expected to be 1 (1:1 Ca:Mn) and for $Ca_3Mn_2O_7$ the ratio is 1.5 (3:2 Ca:Mn). The evolution of the Ca/Mn relative concentration was observed to be strongly dependent on the laser fluence and post-annealing temperatures, as shown in Figure 5a. For low oxygen pressures, without annealing, as the laser fluence increases the Ca/Mn relative percentage starts to increase from approximately 1:1, in $CaMnO_3$, towards the 3:2 proportion as expected from the stabilization of phases with $Ca_3Mn_2O_7$. Nevertheless, the obtained XRD and EDX results indicate the coexistence of the $CaMnO_3$ and $Ca_3Mn_2O_3$ phases in these non-annealed samples at high fluence. The further evolution towards 3:2 is due to the post-deposition annealing step. In this respect, Figure 5b shows the obtained phases, identified from the XRD observed structures and EDS relative Ca/Mn percentage compositions, indicating that, as the annealing temperature increases the $Ca_3Mn_2O_7$ becomes progressively the majority phase, so that for T_{anneal} = 900 ºC only the $Ca_3Mn_2O_7$ phases are present in the films (CMO14 sample).

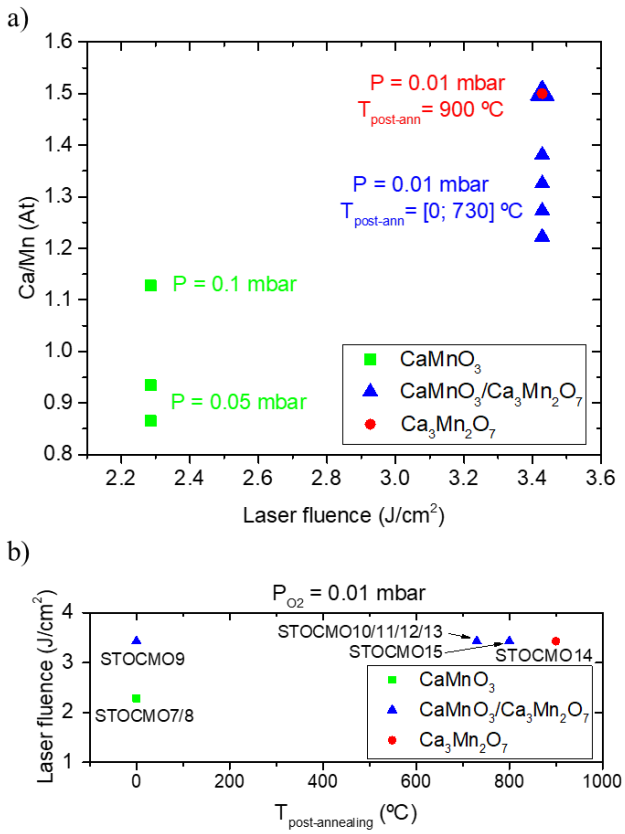

Figure 5: depicted in a) is Ca/Mn atomic ratio represented as a function of the laser fluence applied during the film deposition. In b) are the stabilized phases, depending on the laser fluence and annealing temperature, as obtained from the XRD and EDS results.

As such, considering the results presented above, by using a 700 ºC deposition temperature, 0.01 mbar oxygen pressure and laser fluence of 3.4 J/cm^2, and performing post-deposition annealing in air, at 900 ºC, for 2 hours, allows preparing laser-ablated CMO thin films over $SrTiO_3$ substrates, with the $Ca_3Mn_2O_7$ stoichiometry.

In the X-ray diffraction results of Figure 3, two main $Ca_3Mn_2O_7$ XRD peaks are observed corresponding to the (111), (222) atomic planes. This indicates that the

$Ca_3Mn_2O_7$ films have grown oriented, presenting the [111] direction perpendicular to the substrate plane. Nevertheless, the presence of the small (206) peak in the XRD curves of Figure 3, at $2\theta \sim 44.5^{o}$, indicates a slight degree of polycrystallinity. Since the Acaa phase of $Ca_3Mn_2O_7$ is pseudo-tetragonal [1,5] the observed peaks were used to calculate the lattice parameters using this phase as reference (for the $A2_1am$ an extra peak with a different orientation would be needed). The lattice parameters obtained from the X-ray diffraction peaks observed in the CMO14 film are presented in Table 2 along with the reference Acaa room temperature phase, for comparison. A distortion is observed to occur along the c-axis where a contraction strain was observed, as compared to the reference. On the other hand, the *a* and *b* axis tend to be expanded relative to the bulk. As the polarization of the ferroelectric phase of $Ca_3Mn_2O_7$ is along the *a*-axis [5], the observed distortions indicate that the interfacial substrate/film strain induced on the deposited $Ca_3Mn_2O_7$ films over $SrTiO_3$ substrates promotes the formation of the polar distortion, enhancing the stabilization of the $Ca_3Mn_2O_7$ ferroelectric phase.

Table 2: Lattice parameters of the CMO14 thin film with the $Ca_3Mn_2O_7$ phase.

Phase	**Lattice parameters**				
		Obtained (Å)	**Acaa reference (Å)** [1]	**Deformation strain along growth direction (Acaa)**	**A21am reference (Å)** [1]
$Ca_3Mn_2O_7$	**a**	5.31	5.21189	2.0 %	5.23954
	b	5.31	5.21189	2.0 %	5.23840
	c	19.0	19.59600	-3.0%	19.42711

To further understand the structure and phases of the deposited films Raman spectroscopy was measured in the prepared $Ca_3Mn_2O_7$ samples, at room temperature (T_{RT} = 290 K). Raman spectroscopy yields phonon parameters reflecting the local crystal symmetry, allowing the detection of the presence of structural distortions of the unit cell. Figure 6 shows the Raman spectra measured in the sample CMO14. The observed Raman

modes are identified by B and P symbols according to the notation in reference [14]. The B modes are attributed to the Acaa structure, normally stabilized in $Ca_3Mn_2O_7$ at intermediate temperatures, while the P modes are due to the polar $A2_1am$ low-temperature $Ca_3Mn_2O_7$ phase. There is some degree of overlap between the modes of Acaa and $A2_1am$ structures as the phonon energies anticipated for the $A2_1am$ and Acaa symmetries are nearly degenerate [14]. Nevertheless, in Figure 6, visible modes are due the $A2_1am$ structure were put in the graphic along with the ones for the Acaa structure. Figure 6 indicates the coexistence of the ferroelectric $A2_1am$ and the orthorhombic Acaa phases at room temperature, which has also been observed in bulk $Ca_3Mn_2O_7$ crystals/ceramics [1,15,16].

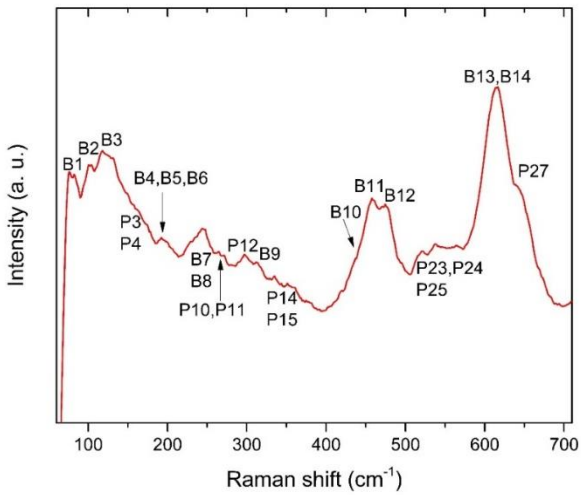

Figure 6: Raman spectrum of CMO14 sample showing $A2_1am$ (marked with P) and Acaa (marked with B) modes.

To further understand the influence of the substrate strain on electric polarization and on coupled magnetic-electric behaviour, the electrical properties of the $Ca_3Mn_2O_7$ films were measured between 30 K and 295 K, region of the stabilization of the ferroelectric phase [1]. In this respect, the dielectric properties are sensitive to polar order/disorder and

cooperative polar behaviour present in a material. Figure 7a shows the temperature-dependent real part of the electrical permittivity at different frequencies. A sharp frequency-dependent step-like change is noted, with decreasing temperature, due to increased polar interactions in the ferroelectric phase, at low temperatures. Figure 7b shows the temperature-dependent imaginary permittivity at the same frequencies measured in CMO14 sample. Here, a peak that shifts to the high temperature with increasing frequency is visible, suggesting a thermally activated behaviour. The peak maximum coincides with the inflection point in the corresponding $\varepsilon'(T)$ curves indicating an intrinsic polar relaxation behaviour [5] In addition, the low values of the loss tangent, with $\tan\delta < 1$, indicate a small contribution of conductivity, due to free charge carriers [17] to the permittivity of the films.

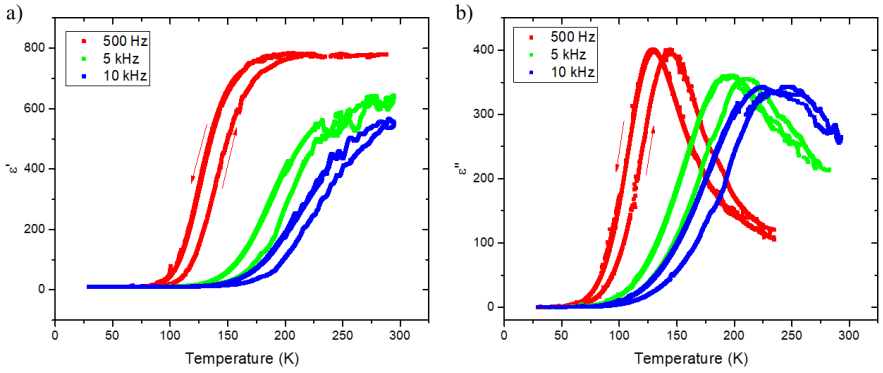

Figure 7: a) Temperature-dependent real permittivity at 500 Hz (red curve), 5 kHz (green curve) and 10 kHz (blue curve). b) Temperature-dependent imaginary permittivity at the same frequencies for CMO14 sample.

Figure 8 presents the real (Figure 8a) and imaginary (Figure 8b) permittivity as a function of frequency at temperatures between 68 K and 242 K measured in the CMO14 film. Two distinct regimes, corresponding to two relaxations, are visible at low and high frequencies marked by a change of slope at low frequencies in the real and in the imaginary parts of the permittivity. The observed relaxations are broad indicating a

distribution of relaxation times and the presence of correlated dipole behaviour. Thus, in order to fit the electrical permittivity curves, the Havriliak-Negami (HN) model function [18,19], with two relaxations was considered:

$$\varepsilon(\omega) = \varepsilon_\infty + \sum_{j=1}^{2} \frac{\Delta\varepsilon_j}{\left[1 + \left(i\omega\tau_j\right)^{\beta_j}\right]^{\gamma_j}} \quad (1)$$

where $\Delta\varepsilon_j$ is the relaxations intensity, ε_∞ is the high-frequency dielectric constant, ω is the angular frequency, τ_j are the relaxations times and β_j and γ_j are coefficients of each HN function, with the constraints $0 < \beta_j \leq 1$ and $0 < \beta_j\gamma_j \leq 1$. For $\beta = \gamma = 1$ the HN model reduces to the Debye function, with only one relaxation time. Equation 1 was fitted to the curves of the real and imaginary permittivity as a function of frequency as shown in Figure 8a and b respectively, to find the function parameters. The corresponding Nyquist plot data with the HN equation fitted is presented in Figure 9. Here, the two distinct regimes corresponding to two relaxations can be seen more clearly.

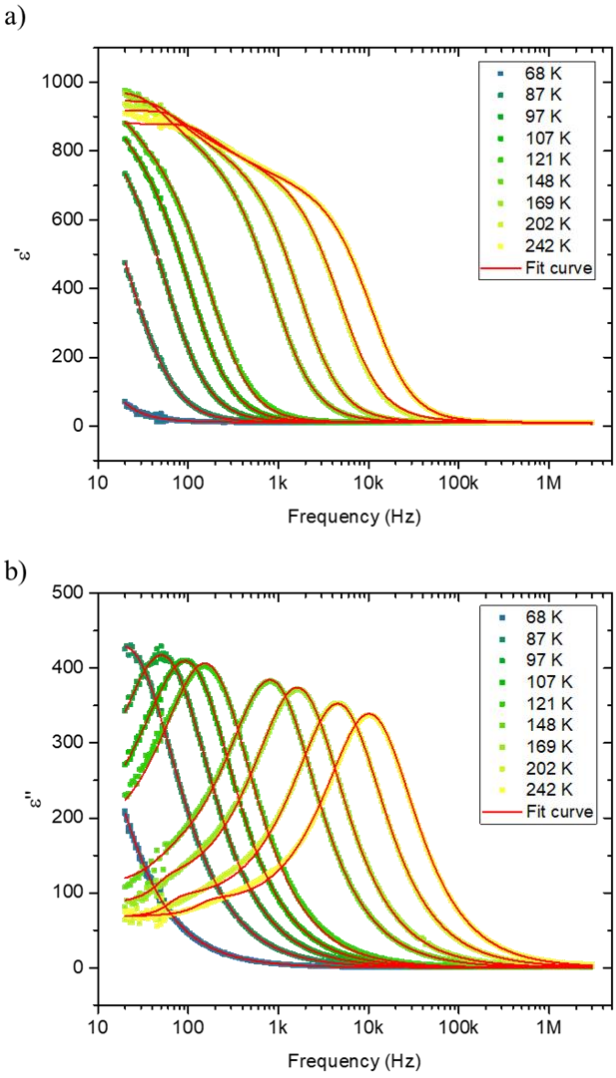

Figure 8: a) Real (a) and imaginary (b) permittivity as a function of frequency at temperatures between 68 K and 242 K with HN equation fit. for CMO14 sample.

a)

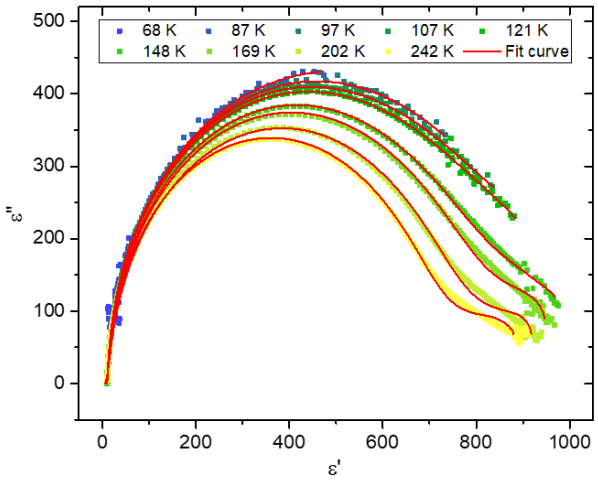

Figure 9: Nyquist plot of the imaginary part as a function of the real part of the complex permittivity at temperatures between 68 K and 242 K with HN equation fit.

The relaxation times obtained from the HN fits for the main relaxation process, occurring at higher frequencies, show a thermally activated temperature-dependent behaviour. As such, to determine the activation energies (E_a), the Arrhenius equation was considered:

$$\tau(T) = \tau_0 e^{\left(\frac{E_a}{k_B T}\right)} \quad (2)$$

Figure 10 shows the logarithm of relaxation times as a function of the inverse of temperature. The graph shows two different regimes, one for temperatures below 121 K in the region where the films become antiferromagnetic (AFM) and the other for temperatures above 148 K. The activation energies were calculated for each regime temperature-dependent, obtaining $E_{a\,\leq 121K} = 0.08\ eV$ and $E_{a\,\geq 148\,K} = 0.05\ eV$.

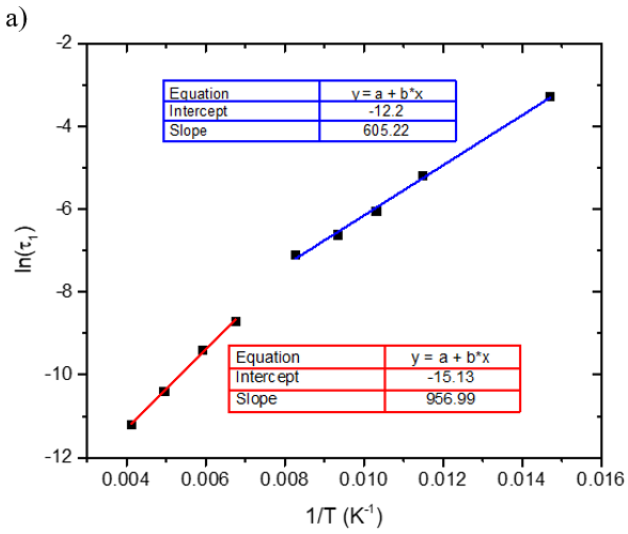

Figure 10: Logarithm of relaxation times as a function of the inverse of temperature with linear fits to the two different regimes, for temperatures below 121 K (blue fit) and temperatures above 148 K (red fit).

Figure 11a shows the temperature dependence of the β and γ parameters, obtained from the fits with the HN function, for the main relaxation in equation 1. The β and γ parameters describe the symmetric and asymmetric broadening of the complex dielectric HN function, respectively. The parameter β increases with increasing temperature, while γ shows the opposite behavior.

The dielectric behavior in the frequency domain is related to that in the time domain by a Fourier transformation. For independent dipoles, with relaxation time τ_D, an exponential decay of the dipole correlation function $\phi(t) = \phi(0)e^{-t/\tau_D}$ is obtained, giving the Debye behavior $\varepsilon(\omega) = \Delta\varepsilon/(1 + i\omega\tau_D)$ in the frequency domain [19]. For a non-Debye relaxation, dipole correlations develop giving a stretched exponential behavior in the time domain described by the Kohlrausch-Williams-Watts (KWW) function:

$$\phi(t) = \phi(0)exp\left(-\left(\frac{t}{\tau_{KWW}}\right)^{\beta_{KWW}}\right) \quad (3)$$

where β_{KWW} is the stretched exponential parameter. β_{KWW} can be connected to the parameters β and γ of the HN function by the relation $\beta_{KWW} = \beta \times \gamma$ [20,21]. Figure 11b shows the temperature dependence of the stretched exponential parameter. An abrupt decrease of β_{KWW} is observed at ~110 K, close to the antiferromagnetic transition temperature of $Ca_3Mn_2O_3$ T_N ~ 112 K [4,5]. The abrupt drop in β_{KWW} across the AFM transition thus indicates the presence of magneto-electric interactions and magnetically induced enhancement of dipolar-correlations with decreasing temperature.

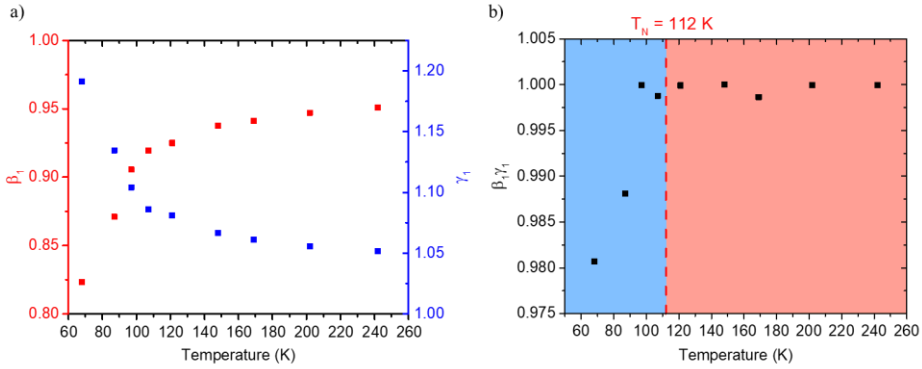

Figure 11: a) Parameter β and γ values obtained for the main relaxation and the product obtained between β and γ parameters. b) Temperature dependence of the stretched exponential parameter, β_{KWW} marked with an abrupt decrease of observed bellow ~110 K.

Compared to $Ca_3Mn_2O_7$ in bulk [22], the thin films analysed here have higher permittivity. This is due to the influence of the Maxwell–Wagner–Sillars polarization that occurs on a nanoscale, where the charge carriers can be blocked at the inner dielectric boundary layers or the interfaces of this films-on-substrate geometry [19].

The magnetic properties of the CMO11, CMO12 and CMO14 samples were measured using a SQUID magnetometer. Figure 12 presents the temperature dependence magnetization (M(T)) under 2500 Oe field. The M(T) curves show that CMO11 and

CMO12 samples have a large paramagnetic component (seen by the Curie type curve, C/T, at low temperatures), added to a diamagnetic background attributed to the substrate. In CMO14 sample, an AFM transition with $T_N \approx 112$ K was found, in accordance with what was observed in the dielectric measurements.

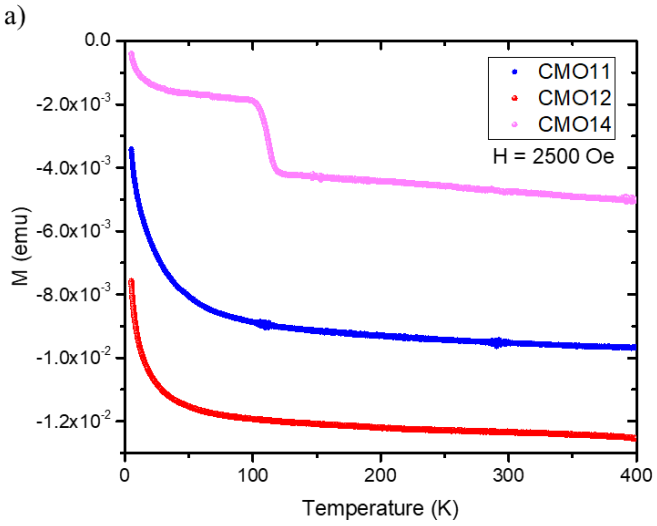

Figure 12: Temperature-dependent magnetization under 2500Oe of CMO11, CMO12 and CMO14 samples, showing an AFM transition with $T_N = 110$ K in CMO14 sample.

References

[1] Rocha-Rodrigues P, Santos S S M, Miranda I P, Oliveira G N P, Correia J G, Assali L V C, Petrilli H M, Araújo J P and Lopes A M L 2020 Ca3Mn2O7 structural path unraveled by atomic-scale properties: A combined experimental and ab initio study *Phys. Rev. B* **101** 64103

[2] Benedek N A and Fennie C J 2011 Hybrid improper ferroelectricity: A mechanism for controllable polarization-magnetization coupling *Phys. Rev. Lett.* **106** 3–6

[3] Lawes G, Benedek N A and Fennie C J 2011 Viewpoint Twisting and turning towards new multiferroics Subject Areas: Materials Science A Viewpoint on: Hybrid Improper Ferroelectricity: A Mechanism for Controllable Polarization-Magnetization Coupling *Phys. Rev. Lett* **4** 107204

[4] Lobanov M V., Greenblatt M, Caspi E N, Jorgensen J D, Sheptyakov D V., Toby B H, Botez C E and Stephens P W 2004 Crystal and magnetic structure of the Ca3Mn2O7 Ruddlesden-Popper phase: Neutron and synchrotron x-ray diffraction study *J. Phys. Condens. Matter* **16** 5339–48

[5] Liu M, Zhang Y, Lin L F, Lin L, Yang S, Li X, Wang Y, Li S, Yan Z, Wang X, Li X G, Dong S and Liu J M 2018 Direct observation of ferroelectricity in Ca3Mn2O7 and its prominent light absorption *Appl. Phys. Lett.* **113** 22902

[6] Nordlander J, Campanini M, Rossell M D, Erni R, Meier Q N, Cano A, Spaldin N A, Fiebig M and Trassin M 2019 The ultrathin limit of improper ferroelectricity *Nat. Commun.* **10** 1–7

[7] Baghizadeh A, Vaghefi P M, Huang X, Borme J, Almeida B, Salak A N, Willinger M, Amaral V B and Vieira J M 2021 Interplay of Magnetic Properties and Doping in Epitaxial Films of h-REFeO3 Multiferroic Oxides *Small* **17** 2005700

[8] Varignon J, Vila L, Barthélémy A and Bibes M 2018 A new spin for oxide interfaces *Nat. Phys.* **14** 322–5

[9] Lu X Z and Rondinelli J M 2016 Epitaxial-strain-induced polar-to-nonpolar transitions in layered oxides *Nat. Mater.* **15** 951–5

[10] Ghidini M, Mansell R, Maccherozzi F, Moya X, Phillips L C, Yan W, Pesquera D, Barnes C H W, Cowburn R P, Hu J M, Dhesi S S and Mathur N D 2019 Shear-strain-mediated magnetoelectric effects revealed by imaging *Nat. Mater.* **18** 840–5

[11] Molinari M, Tompsett D A, Parker S C, Azough F and Freer R 2014 Structural, electronic and thermoelectric behaviour of CaMnO3 and CaMnO(3-δ) *J. Mater. Chem. A* **2** 14109–17

[12] Ablitt C, Mostofi A A, Bristowe N C and Senn M S 2018 Control of uniaxial negative thermal expansion in layered perovskites by Tuning layer thickness *Front. Chem.* **6** 455

[13] Guiblin N, Grebille D, Leligny H and Martin C 2002 Ca3Mn2O7 *Acta Crystallogr. Sect. C Cryst. Struct. Commun.* **58**

[14] Glamazda A, Wulferding D, Lemmens P, Gao B, Cheong S W and Choi K Y 2018 Soft tilt and rotational modes in the hybrid improper ferroelectric Ca3Mn2O7 *Phys. Rev. B* **97** 94104

[15] Spaldin N A and Ramesh R 2019 *Advances in magnetoelectric multiferroics* vol 18(Nature Publishing Group)

[16] Trassin M 2016 Low energy consumption spintronics using multiferroic heterostructures *J. Phys. Condens. Matter* **28** 33001

[17] Raghavender A T, Samantilleke A P, Sa P, Almeida B G, Vasilevskiy M I and Hong N H 2012 Simple way to make Anatase TiO2 films on FTO glass for promising solar cells *Mater. Lett.* **69** 59–62

[18] Havriliak S and Negami S 1967 A complex plane representation of dielectric and mechanical relaxation processes in some polymers *Polymer (Guildf).* **8** 161–210

[19] Kremer F (Friedrich) and Schönhals A (Andreas) 2003 *Broadband dielectric*

spectroscopy (Springer)

[20] Alvarez F, Alegra A and Colmenero J 1991 Relationship between the time-domain Kohlrausch-Williams-Watts and frequency-domain Havriliak-Negami relaxation functions *Phys. Rev. B* **44** 7306

[21] Górska K, Horzela A, Bratek L, Dattoli G and Penson K A 2018 The Havriliak–Negami relaxation and its relatives: the response, relaxation and probability density functions *J. Phys. A Math. Theor.* **51** 135202

[22] Sahlot P, Sharma G, Sathe V, Sinha A K and Awasthi A M 2020 Interplay of spin, lattice, vibration, and charge degrees of freedom: Magneto-dielectricity in Ca3Mn2O7 *J. Am. Ceram. Soc.* **103** 3238–48